

# The effect of metal dissolution on carbon production by high-temperature molten salt electrolysis

Emma Laasonen<sup>a,\*</sup>, Miika Sorvali<sup>c</sup>, Vesa Ruuskanen<sup>b</sup>, Markku Niemelä<sup>b</sup>, Tuomas Koiranen<sup>a</sup>, Jero Ahola<sup>b</sup>, Jyrki M. Mäkelä<sup>c</sup>, Tero Joronen<sup>d</sup>

<sup>a</sup> School of Engineering Science, LUT University, P.O. Box 20, FI-53851 Lappeenranta, Finland

<sup>b</sup> School of Energy Systems, LUT University, P.O. Box 20, FI-53851 Lappeenranta, Finland

<sup>c</sup> Aerosol Physics Laboratory, Faculty of Engineering and Natural Sciences, Tampere University, Tampere, Finland

<sup>d</sup> Materials Science and Environmental Engineering, Faculty of Engineering and Natural Sciences, Tampere University, Tampere, Finland

## ARTICLE INFO

### Keywords:

Molten salt electrolysis  
Carbonate salt  
Electrochemical cell  
Nano-onions  
Nanotubes  
CO<sub>2</sub> utilization

## ABSTRACT

High-temperature molten salt electrolysis is suitable for the production of carbon morphologies such as carbon nanotubes and nano-onions. In this study, CO<sub>2</sub> was electrochemically reduced to solid carbon by molten lithium carbonate electrolysis in an Inconel 625 vessel at a fixed temperature of 750°C. Four different cathodes (clean nickel, used nickel, stainless steel, and galvanized steel) were used to determine the effect of the electrode material on the morphology produced. The carbonaceous products obtained were analyzed with scanning electron microscopy (SEM), transmission electron microscopy (TEM), energy-dispersive X-ray spectroscopy (EDS), Raman microscopy, and X-ray diffraction (XRD). With nickel cathodes, the dominant forms of carbon were spherical, whereas tubular structures dominated with steel-based cathodes. Nano-onion was the structure of carbon with the least metal impurities. Iron was discovered to promote carbon nanotube growth. In the presence of iron, nanotube wool was also found. A greater number of different morphologies were observed when the amount of metal impurities increased. The correlation found between XRD results and sample masses suggests that the amount of metal impurities in the sample varied more than the carbon content. Thus, the yield of the process can be expected to be fairly similar between parallel experiments.

## 1. Introduction

High-temperature molten salt electrolysis is suitable for the production of various forms of solid carbon from CO<sub>2</sub>. For example, carbon nanotubes (CNTs) [1–5], nanofibers (CNFs) [6], nano-onions (CNOs) [7], nanoplatelets [8,9], nanoscaffolds [10], porous carbon [11,12], and carbon powders [13–15] have been produced by this method. Moreover, previous experimental works, e.g. [16,17], and [18] have drawn attention to the possibility of producing carbon monoxide from CO<sub>2</sub> using this electrolytic approach.

Various process parameters have been reported to affect the carbon morphology, as shown in Table 1. A comprehensive literature review of molten salt electrolysis and the effects of process parameters on carbon production is given in [19]. Other reviews addressing CO<sub>2</sub> conversion technologies utilizing molten salts can be found in for example [20,21] and [22].

Although different process parameters are already known to affect

the carbon morphology, more research about consequential parameters is nevertheless required. Previous publications concerning this topic, e.g. publications in Table 1, have focused on the effect of process parameters such as current density and temperature. It is already known that certain metals, e.g. iron and zinc, can nucleate nanotube growth when other carbon syntheses are used [25]. Previous studies, for example [6], indicate that different metals can possibly nucleate the formation of a specific type of carbon morphology also in molten carbonate salt electrolysis.

The objective of the research reported in this paper was to determine how different metals released from the electrodes during electrolysis affect the carbon produced at otherwise fixed conditions. Previous publications such as [26] and [27] have considered various cathode materials, but simultaneously e.g. anode material and current density have been changed. Thus, this seems to be the only publication that focuses only on the effect of the cathode material. To determine how different metals affect the carbon morphology, various cathode

\* Corresponding author.

E-mail address: [emma.laasonen@lut.fi](mailto:emma.laasonen@lut.fi) (E. Laasonen).

<https://doi.org/10.1016/j.jcou.2023.102390>

Received 4 October 2022; Received in revised form 17 November 2022; Accepted 2 January 2023

Available online 9 January 2023

2212-9820/© 2023 The Author(s). Published by Elsevier Ltd. This is an open access article under the CC BY license (<http://creativecommons.org/licenses/by/4.0/>).

**Table 1**

The effect of various process parameters on carbon produced by high-temperature molten salt electrolysis.

Parameter	Effect	Ref.
Electrolysis time	Higher temperature increases particle size and porosity.	[14]
	With higher temperatures more of the product is CO instead of solid carbon.	[16]
	More tubular structures are produced as electrolysis time increases.	[8]
	Crystallinity increases with increase in electrolysis time.	[7]
	Carbon nanotube diameter increases with increase in the electrolysis time.	[23]
Current density	Current density has no evident effect on product morphology.	[23]
	Current density has some effect on particle size and platelet thickness.	[23]
	Higher voltage leads to smaller particle size.	[24]
Voltage	Higher voltage leads to greater surface area / higher porosity.	[24]
	Without oxides in the electrolyte, the tubular product is straight.	[2,3,6]
Oxide concentration	With oxides in the electrolyte, the tubular product is tangled.	[2,3,6]
	Nucleation promotes carbon deposition.	[7]
Nucleation step	Diffusion controls whether the product is carbon nanotubes or nanofibers.	[3]
Diffusion control		

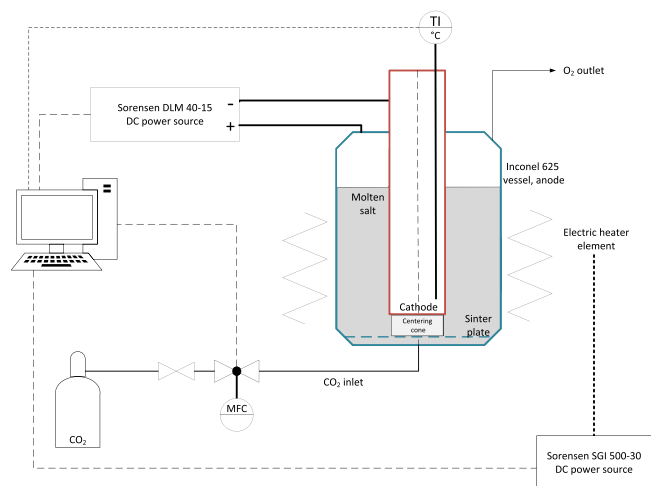


**Fig. 1.** Piping and instrumentation diagram of the reactor unit (not in scale). The thermocouple inside the cathode was placed 30 mm from the bottom. The molten electrolyte height is calculated to be 49 mm. CO<sub>2</sub> is fed through the sinter plate placed at the bottom of the reactor.

materials were selected for the experimental study, namely clean nickel, used nickel, stainless steel, and galvanized steel. To date, to the best of authors' knowledge, there have been no studies which focuses merely on the effect of various cathode materials on this specific molten carbonate salt electrolysis process.

## 2. Materials and methods

### 2.1. Reaction mechanism

The cathodic and anodic reactions of electrochemical reduction of CO<sub>2</sub> to solid carbon, respectively, in the presence of a carbonate are [28]:

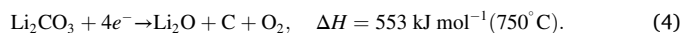


Thus, the total reaction is:

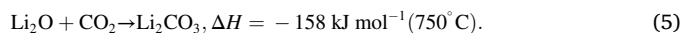


An alternative viewpoint is to consider the reactions occurring through the reactions of lithium carbonate, as has been done e.g. by Lau et al. [29].

Lithium carbonate decomposes as:



Produced Li<sub>2</sub>O is replenished to lithium carbonate as in the following:



The carbon production rate (mol s<sup>-1</sup>) is linearly dependent on the current:

$$\dot{n} = \eta_F \frac{I}{Z F}, \quad (6)$$

where  $\eta_F$  is the Faraday efficiency or current efficiency,  $I$  is the electric current,  $n$  is the amount of substance in moles,  $Z$  is the number of electrons transferring, and  $F$  is Faraday's constant. In the experiments in this paper, the current used was 7.5 A, the electrolysis time was 90 min (5400 s), and the number of electrons transferring, according to Eq. (4), was 4. Calculated from Eq. (6), the theoretical amount of solid carbon produced during 90 min electrolysis is 1.26 g. When the  $U/I$  sequence run prior to the actual electrolysis is taken into account, the total theoretical maximum amount of carbon produced is 1.47 g. The  $U/I$  sequence comprised steps of 0.1 A, 1 A, 5 A, 10 A, 5 A, 1 A, and 0.1 A, with the duration each of the steps being 5 min. More details about the  $U/I$  sequence can be found from the Supplementary Material.

### 2.2. Reactor unit

A cylindrical reactor vessel made of Inconel 625 was placed inside an oven (Goldbrunn 1000). Inconel 625 was selected as the anode material based on its presumed good stability as an anode material in molten carbonate salt electrolysis [30]. The vessel had an inner diameter of 50.8 mm, and it acted as an anode during the electrolysis. The surface area of the anode in the salt was 100 cm<sup>2</sup>. Cathodes were made of nickel, galvanized steel, or stainless steel. The diameter of each cathode was 30 mm and the height 150 mm. The surface area of the cathode in the salt was 50 cm<sup>2</sup>. Sizing of the reactor and its parts was limited by the size of the oven. A piping and instrumentation diagram of the experimental setup is shown in Fig. 1. The measurement and control units used were the same as used in [19].

### 2.3. Procedure

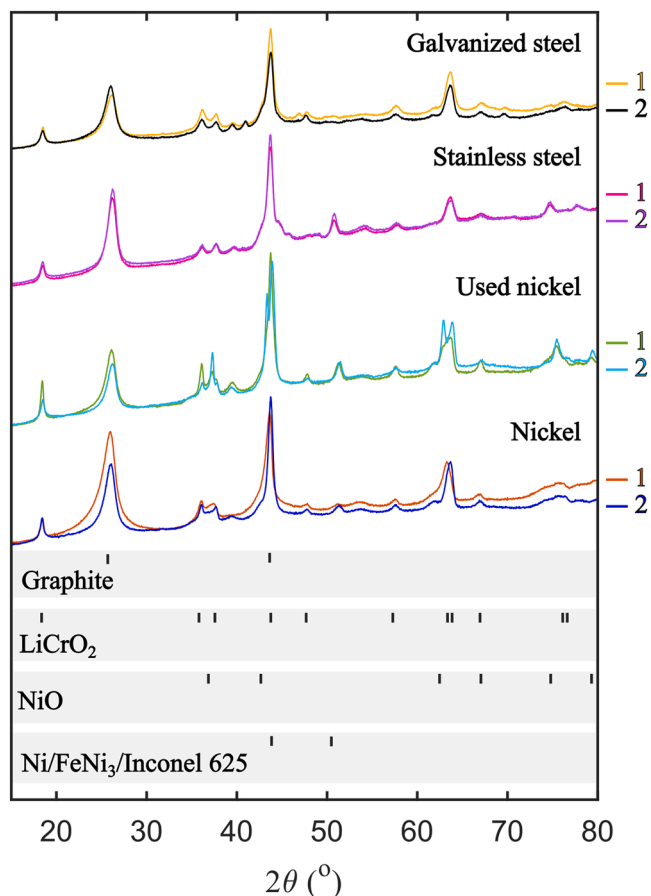
Experiments were conducted with four different types of cathodes; unused nickel, stainless steel, galvanized steel (zinc coated stainless steel), and used nickel, respectively. The same nickel cathodes were used twice. The first time using the cathode is referred as "unused" and second as "used". Two subsequent experiments were conducted with each type of electrode. The temperature inside the cathode was measured during the electrolysis, as well as cell voltage. The electrolysis was run for 90 min at a set temperature of 750°C. The cathode temperature remained very close to the set value of 750°C during all the experiments. The oven heating power was controlled during the experiments to maintain desired temperature. Cell voltages varied in the range of 1.8 V–3.6 V while the current was kept constant at 7.5 A. This current applied is equivalent to the cathode current density of 0.15 A cm<sup>2</sup>.

Prior to electrolysis, a current sequence was run to determine the  $U/I$  curves. During the electrolysis, CO<sub>2</sub> was fed at a rate of 30 mL min<sup>-1</sup> at

**Table 2**

Analysis methods previously utilized to analyze carbon particles.

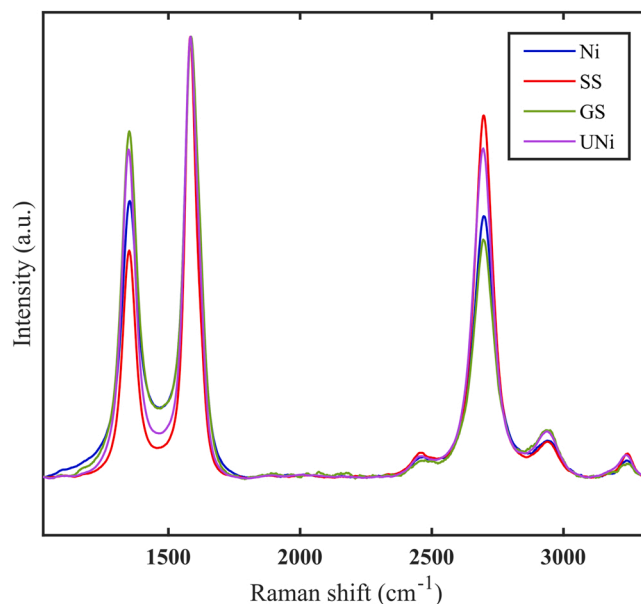
Carbon identified	Analysis method used								Reference
	SEM	EDS	TEM	Raman	XRD	AFM	BET	FTIR	
CNT, CNF	x	x	x	x					[2]
CNT	x	x		x	x				[6]
CNT	x	x	x						[30]
CNT			x	x	x				[1]
CNO, CNT	x	x	x	x	x				[7]
Platelet	x		x	x	x	x			[8]
Carbon powder	x	x		x	x		x	x	[24]
Various structures	x	x	x	x			x		[23]

**Fig. 2.** XRD patterns of the washed samples. The number of the sample is marked on the right side of the figure, and the most significant peaks for the main identified phases at the bottom of the figure.

standard conditions. This feed rate was calculated to be sufficient for the carbon production based on Eq. (3) and Eq. (6). The accumulated sample was mechanically removed from the cathode surface and washed with hydrochloric acid to remove the electrolyte from the carbon. The washed sample was rinsed with deionized water and dried in an oven at 105°C. A more detailed description of the procedure and the temperature, voltage and  $U/I$  curve measurements can be found in the Supplementary Material.

#### 2.4. Analysis methods

Many different analysis methods are applicable for the analysis of the structure of solid particles. In previous literature, at least methods listed in Table 2 have been utilized in analyzing solid carbon products obtained from molten salt electrolysis.

**Fig. 3.** Raman patterns of the samples with different cathodes scaled to match the G band peak at 1585 cm<sup>-1</sup>. Ni refers to nickel, SS to stainless steel, GS to galvanized steel, and UNi to used nickel.

Based on previous literature analysis methods concluded to be most suitable were scanning electron microscopy (SEM), transmission electron microscopy (TEM), energy-dispersive X-ray spectroscopy (EDS), Raman microscopy, and X-ray diffraction (XRD). Using all these five methods enables a comprehensive understanding of the product is obtained. The XRD analysis was performed with a Panalytical Empyrean X-ray diffractometer using monochromatized CuK $\alpha$  radiation in the measurement range 15° < 2 $\theta$  < 80°. A Renishaw inVia™ Qontor® Raman microscope was used for measuring spectra from single points and also measuring Raman maps from several hundred locations, whose results were averaged over the measured patterns. Wavelength of 532 nm and laser power of 0.3 mW were used. A JEOL JEM-F200 microscope with an added energy-dispersive (EDS) detector was used for the transmission electron microscopy. The Zeiss UltraPlus FE-SEM used for SEM imaging also contained an EDS detector for observing different elements.

### 3. Results and discussion

#### 3.1. XRD

The XRD patterns (Fig. 2) reveal various impurity compounds mixed with the carbon produced. These impurity phases originate from material released from the electrodes during the electrolysis, as the metals identified have no other possible source.

The carbon is mostly represented by the main graphite peak at around 26°. Graphite also has a minor peak (ca. 15% of the main peak



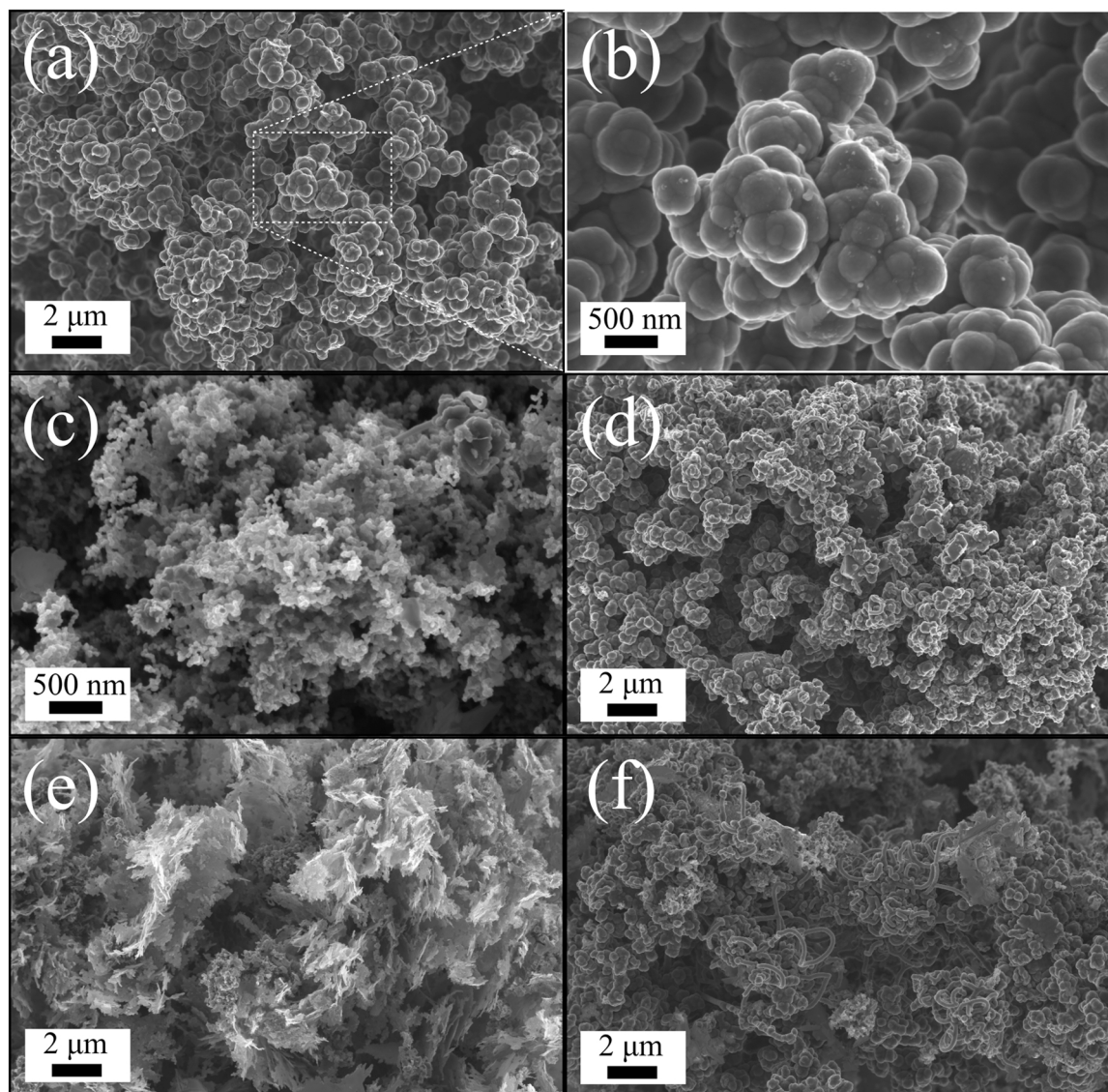


**Fig. 4.** SEM images of nickel cathode samples: (a) the major morphology of nano-onions found in the samples, (b) a higher magnification of the nano-onions, (c) significantly smaller spherical structures, (d) more irregular shapes, (e) platy structures, and (f) tubular structures.

intensity) at around  $44^\circ$ . However, this peak could not be distinguished, as it was covered by contributions from other compounds. Amorphous carbon has been observed to produce wide features in the XRD patterns, especially with lower incidence angles [14]. Since no significant wide peaks could be observed, most of the carbon is presumed to be crystallized. A more indicative representation of the graphitization degree of the carbon is obtained with Raman spectroscopy.

The most significant impurity phase identified was  $\text{LiCrO}_2$ , which was found in all the samples. This phase is formed from chromium, released from the Inconel anode, reacting with the molten lithium salt.  $\text{LiCrO}_2$  produces several peaks, strongest of them being at around  $18^\circ$ ,  $36^\circ$  and  $44^\circ$ . All significant peaks are marked in Fig. 2. Another impurity phase, which was especially noticeable in the used nickel sample 2, was nickel oxide. NiO has the strongest reflections at around  $37^\circ$ ,  $43^\circ$  and  $63^\circ$ . The last phase marked in Fig. 2 is a mixture of three possible phases, Ni,  $\text{FeNi}_3$  and Inconel 625, which have their main peaks very close to each other at roughly  $44^\circ$  and  $51^\circ$ . They are thus almost impossible to tell apart based on XRD measurements. Another minor phase identified in all the samples, though not marked in the figure, was  $\text{Mo}_2\text{C}$  represented by a low intensity peak at around  $39^\circ$ . Molybdenum is a minor component in the anode material Inconel 625, thus its presence in the samples

is to some extent expected. In addition, some minor impurity phases likely stayed unidentified. Especially the strong reflection at around  $63^\circ$  likely has another contributor in addition to  $\text{LiCrO}_2$ . Nevertheless, a great majority of the impurities can be considered to have been accurately identified. Fractions of the impurities, however, would require Rietveld analysis, which is very difficult in a strongly mixed sample like this with unidentified phases.

### 3.2. Raman microscopy

To support XRD results Raman measurements were conducted. Only one of the two parallel samples was studied in each case. Fig. 3 shows the Raman patterns obtained by measuring maps of several hundred points and averaging over the obtained patterns. Backgrounds were computationally subtracted, and all of the patterns scaled to match the G band peak intensity at around  $1585\text{ cm}^{-1}$  to help compare the peak intensity ratios. While the other samples produced almost exclusively good measurement points, the galvanized steel sample exhibited significant luminescence, which corrupted half of the measured patterns.

The Raman patterns include three main peaks: the D band at around  $1350\text{ cm}^{-1}$  that arises from disorder, the G band at around  $1585\text{ cm}^{-1}$ ,



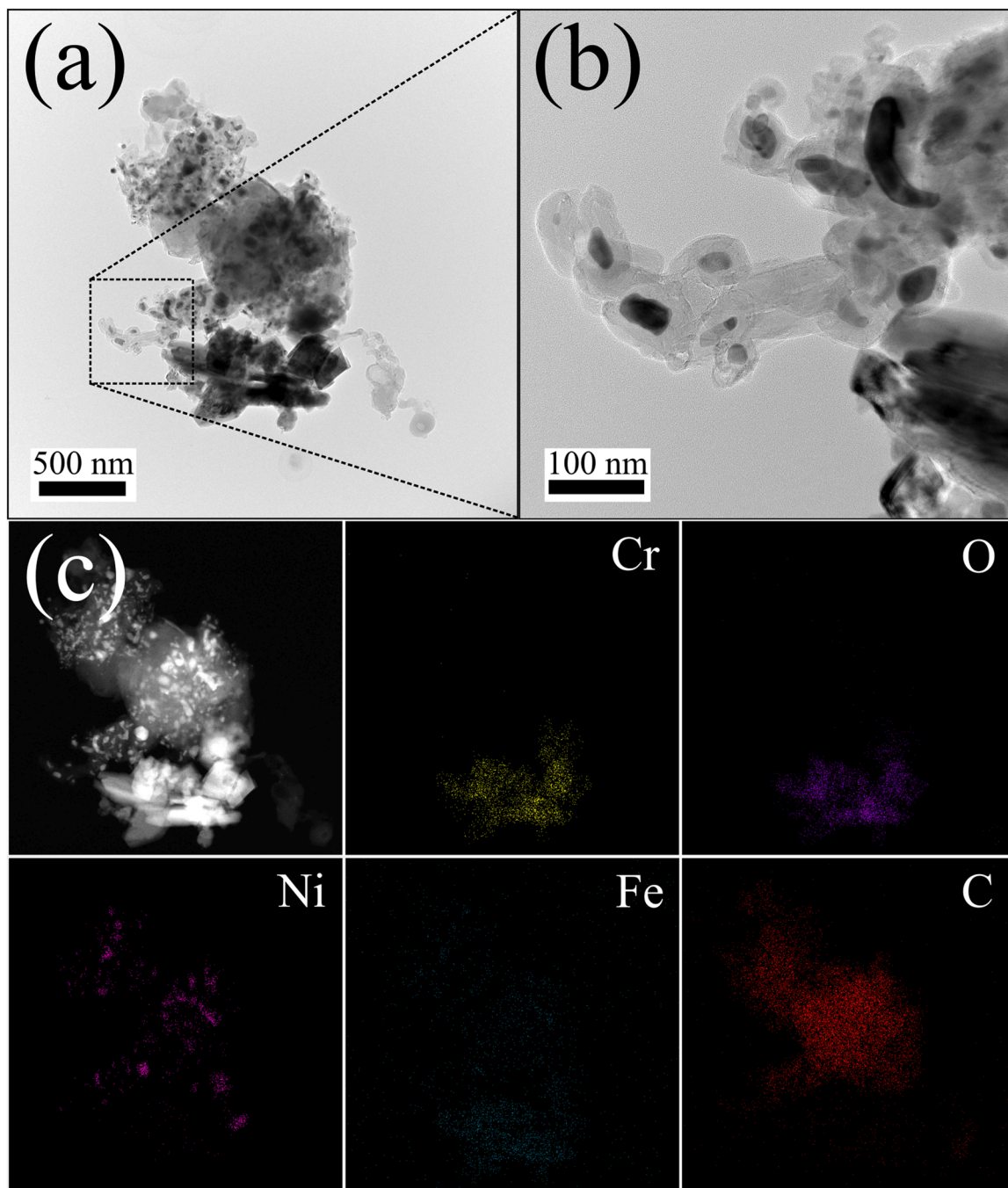


**Fig. 5.** TEM images of (a) and (b) a typical agglomerate in the nickel sample at two different magnifications, and (c) EDS maps of agglomerate for different elements.

referring to the first order  $E_{2g}$  mode, and the  $G'$  (sometimes referred to as 2D band, as it is the second order mode of D) at around  $2695\text{ cm}^{-1}$  [31]. In addition, a few minor peaks often arise with carbon materials. One of them is a disorder-induced  $D'$  peak at around  $1620\text{ cm}^{-1}$ , covered by the G band in this case, and its overtone  $2D'$  found at around  $3240\text{ cm}^{-1}$ . Additionally, two peaks arise from combinations of two phonons ( $D + D''$  and  $D + D'$ ) at roughly  $2460$  and  $2940\text{ cm}^{-1}$ , respectively [32].

The G and the D bands can be used to assess the degree of graphitization in carbon samples. The lower the intensity ratio between the D and G bands ( $I_D/I_G$ ), the more the well-ordered structures are considered to dominate the material [1,6,7]. The  $I_D/I_G$  ratio was 0.63 for the new nickel, 0.74 for the used nickel, 0.51 for the stainless steel, and 0.78 for the galvanized steel.

The ratios imply that all of the samples are quite well graphitized,

though differences between the samples were observed. Stainless steel seems to produce the highest degree of graphitization, which implies the lowest number of defects. When the two nickel cathodes are compared, the corrosion of the electrodes seems to lower the product quality, as the number metallic of impurities increases. This in turn leads to more defects in the carbon structures.

The  $G'$  peak can be linked to the number of layers and the layer stacking of the structures [31]. However, the relationship is not yet perfectly understood. Graphene structures consisting of 1–4 layers can be quite well distinguished based on the peak profile, but structures with more than 5 layers tend to produce a profile very similar to graphite [33]. Therefore, the peak profile cannot be exploited here. However, there has been some indication that the  $G'$  peak intensity might decrease as the layer thickness grows [31]. If the two different nickel cathodes are

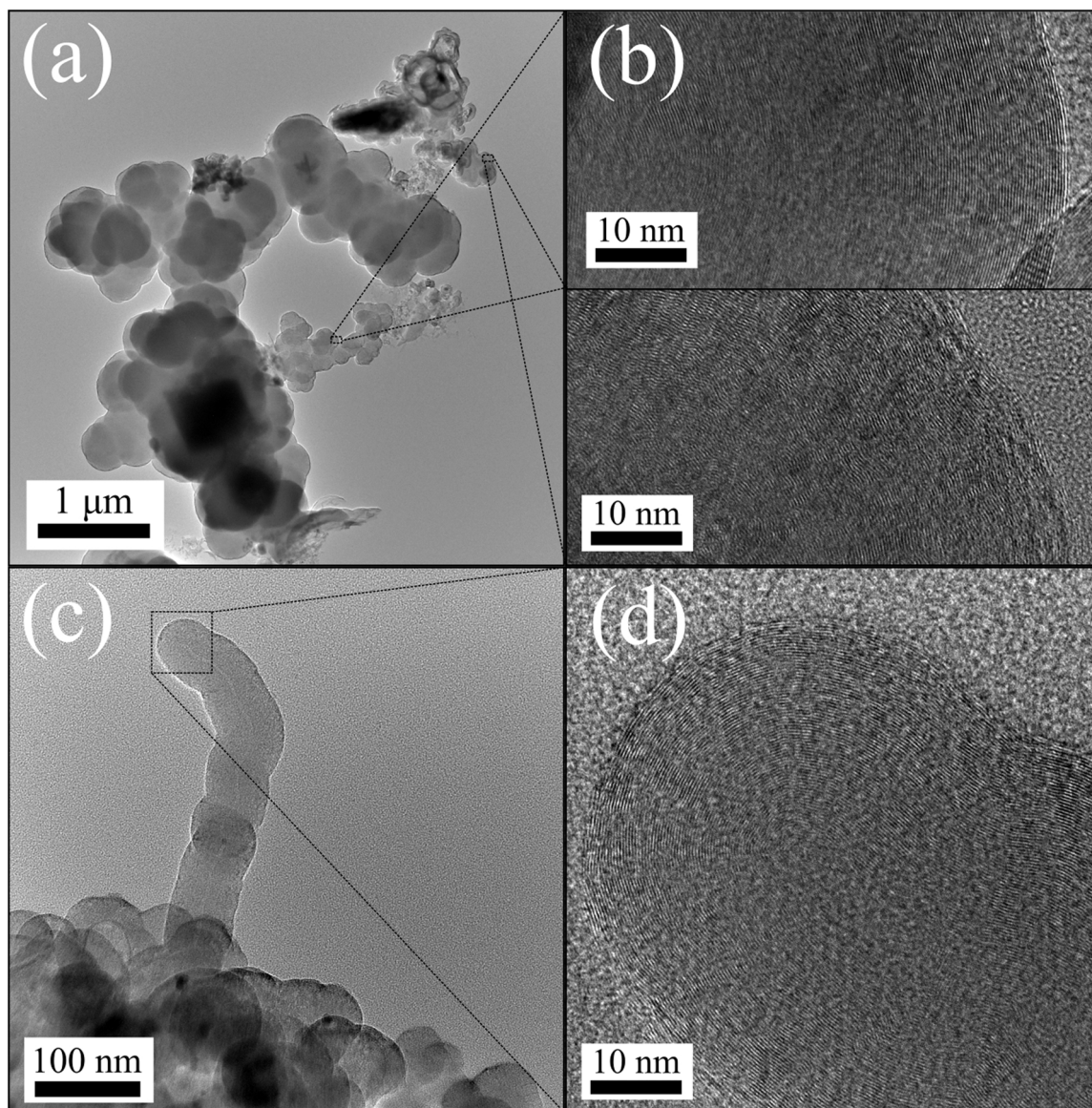


**Fig. 6.** TEM images of (a) and (b) a cauliflower-like nano-onion structure in the nickel sample with two different magnifications, and (c) and (d) a chain-like nanotube at two different magnifications.

compared, this type of a difference might be expected based on the XRD results. One would expect the sample with a higher volume of impurities (used nickel) to produce thinner structures, since more of the carbon grows onto the impurity particles. This would then be reflected in the higher  $G'$  peak.

### 3.3. Electron microscopy

#### 3.3.1. Nickel cathode

The SEM images of nickel cathode samples showed the largest variety of morphologies out of the selected cathodes. Fig. 4 shows SEM images of various structures found in the nickel samples.

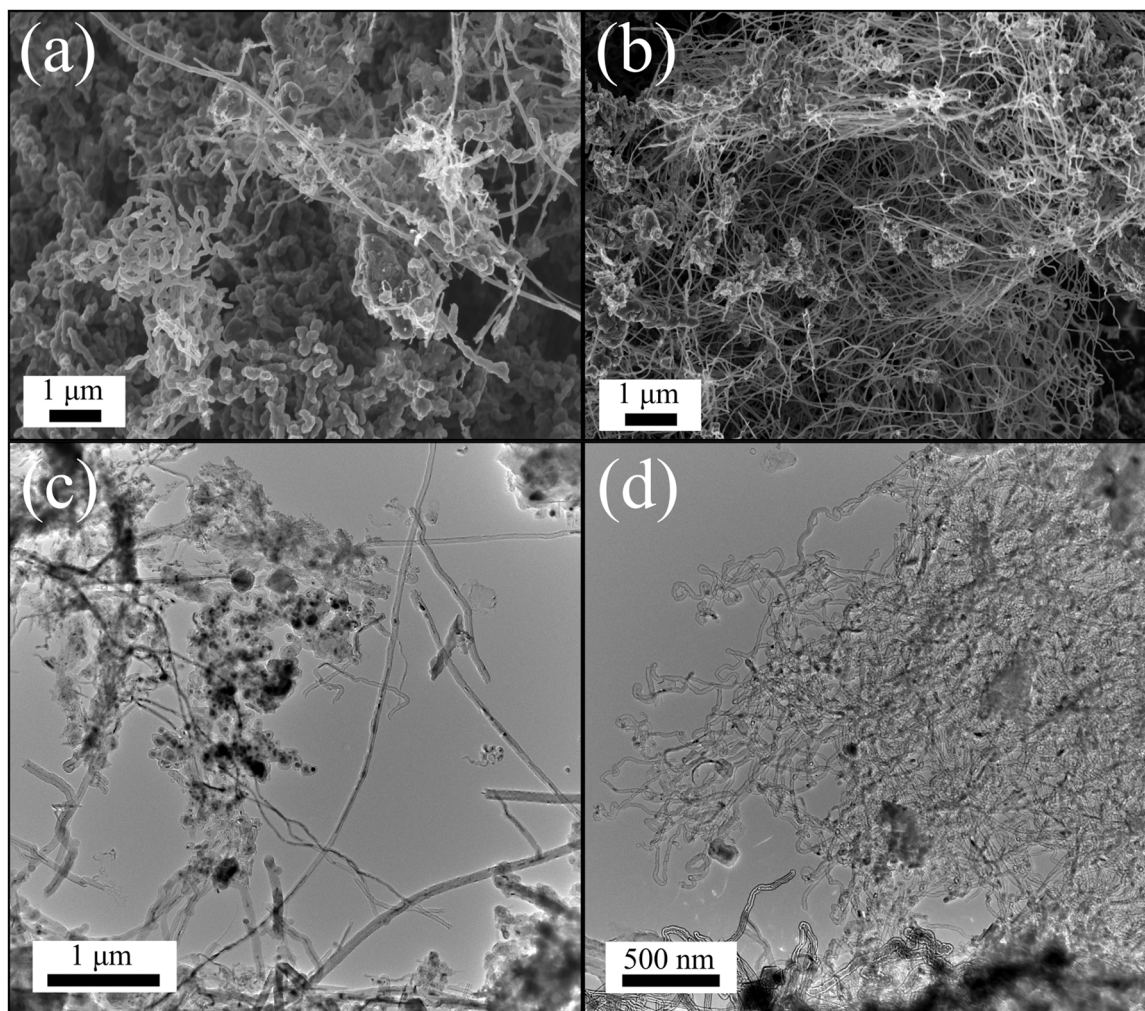
Figs. 4a and 4b show different magnifications of similar cauliflower-like nano-onion structures that were previously reported by Laasonen et al. [19]. The EDS measurements suggest that these structures seem to be relatively free of impurities (Fig. S1a and S1b)). Although these types of structures were the most prevalent, other morphologies were also found. Fig. 4d presents an area somewhat similar to the nano-onions, but with smaller structures and mixed with more irregular shapes, some chain-like structures, and even some octahedral shapes.

Fig. 4c shows an area consisting of still smaller spherical nanostructures, Fig. 4e mostly nanoplates, and Fig. 4f an area with more tubular structures. In addition to these nanostructures, a significantly larger piece in the size range of tens of micrometers was found. The piece was confirmed to mostly consist of very tightly packed spherical carbon structures (Fig. S1c and S1d). This finding suggests that some of the pure carbon structures form denser and larger pieces compared to most of the structures described here.

The TEM images offer more detailed information on the structures. As the XRD results showed, a significant portion of the material contained impurities. Fig. 5 presents TEM images of a typical irregularly shaped agglomerate found in the nickel sample, along with EDS maps for different elements.

The TEM images reveal that a significant part of the carbonaceous material grew on top of impurities acting as seed particles. There also seems to be a wide size range of impurity particles, all of which are covered with a carbon envelope. Fig. 5c shows EDS maps for different elements in the agglomerate. The most significant EDS signals for the large impurity particles originated from chromium and oxygen. Since no chromium oxide was detected by XRD, and lithium is too light an





**Fig. 7.** SEM images of (a) more spherical structures mixed with nanotubes and (b) nanotube wool, and (c) and (d) TEM images roughly corresponding to the structures in (a) and (b).

element to be detected by EDS, the signal can be interpreted as being related to the LiCrO<sub>2</sub>. The small nanometer-range bits were mostly identified as nickel. A rather weak iron signal could also be found across the whole sample, which might indicate iron dissolving in ion form and being transported to several locations. It is rather challenging to explicitly disclose the form of iron at every location of the sample.

As Fig. S2 shows, some of the pieces containing Cr and O also gave a significant Fe signal, likely indicating a piece of Inconel 625 released from the anode. Also, some of the small nickel pieces showed a clear presence of iron, which could refer to FeNi<sub>3</sub>. These results suggest that the peaks in XRD patterns assigned to Ni/FeNi<sub>3</sub>/Inconel 625 could actually arise from all three of these components in an unknown ratio. Since these particles seem to be a lot smaller compared to LiCrO<sub>2</sub> particles, the lower relative contribution to the XRD patterns is understandable.

The EDS measurements performed alongside the SEM imaging showed that the nano-onions consisted of virtually pure carbon. Fig. 6a presenting nano-onions supports this conclusion, since most of the structure does not seem to have impurity particles in the core. Therefore, these structures can be considered to represent the purest form of carbon produced in the process. Seed particles with varying sizes and shapes led to a large range of shapes and sizes also for the final particles. The closer magnification images in Fig. 6b reveal that both straight and wavy atomic planes are present in the nano-onions.

Fig. 6c and 6d show a close-up image of a chain-like structure. This

tube seems to have grown in separate parts from a very fine seed particle by both tip growth and root growth mechanisms [34]. A small seed particle can be found in the middle of the tube. Due to the small size, the composition could not be confirmed with EDS, though it is presumed to be a nickel particle due to results of other analyses conducted. The lower part the tube structure seems to have grown under the seed particle, and the top part on top of it. The tip of the tube indicates that different parts of the structure are very well graphitized. Additional TEM images are given in Fig. S3.

### 3.3.2. Used nickel

Based on SEM imaging, the used nickel samples contained mainly similar structures to the unused nickel samples, with the exception of the nano-onions being the most common morphology (Fig. S4). Since the used nickel cathodes seemed to release more material than the unused nickel cathodes, and the samples were also produced with the most worn anode, the effect of impurities was also clearly more visible in the structures. This observation correlates with the XRD results.

Most of the sample area was dominated by very mixed morphologies (Figs. S4a and S4b), and needle-like impurity particles, in particular, could be found throughout the sample (Fig. S4f). EDS measurements confirmed that the areas with highly mixed morphologies contained significant amounts of nickel and chromium (Fig. S4c). A large piece (hundreds of  $\mu$ m) of partly oxidized nickel was also found (Figs. S4d and S4a). As these large particles have a high volume, and therefore a big



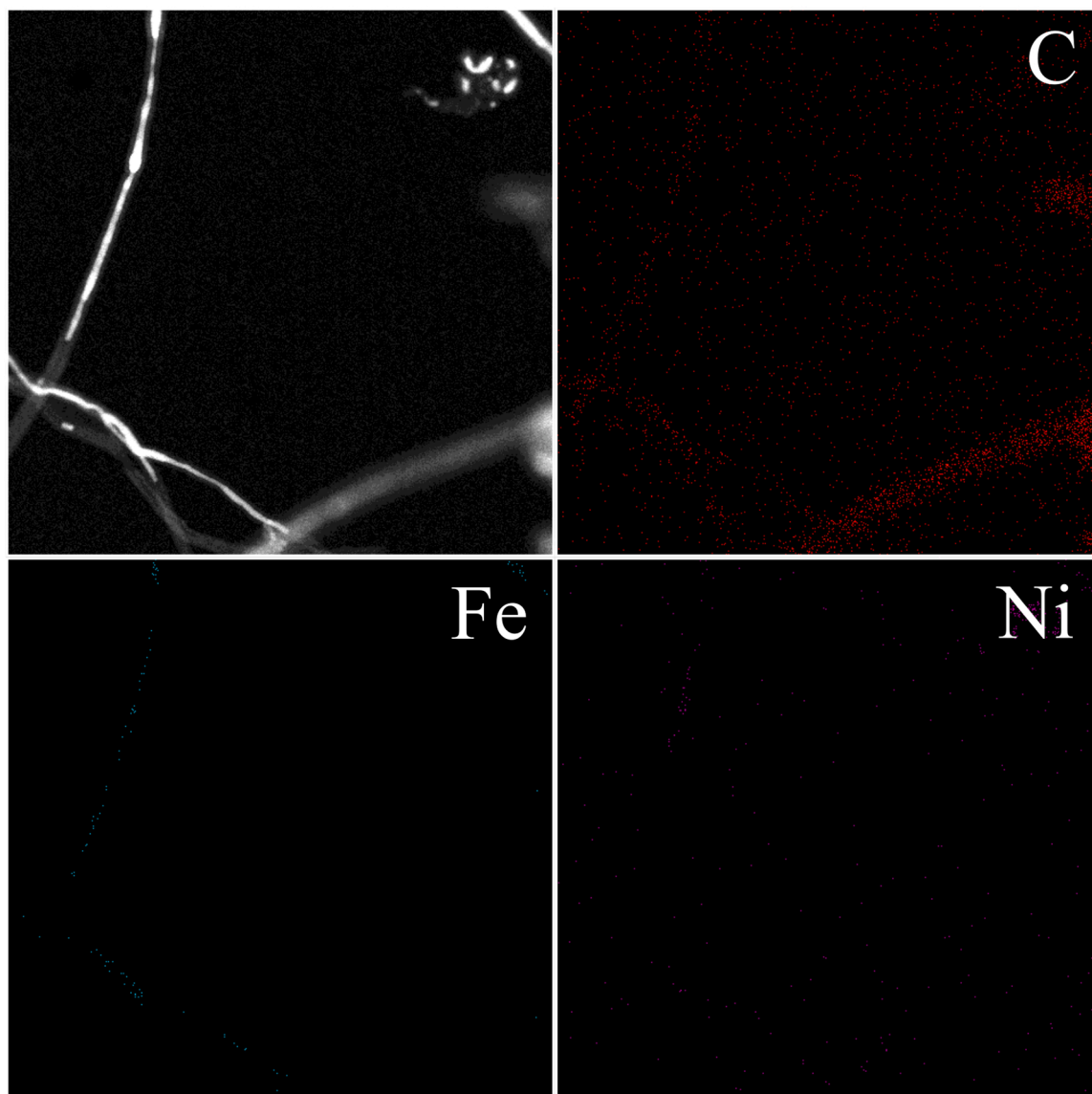


Fig. 8. EDS maps of C, Fe and Ni for some nanotubes in the stainless steel sample.

impact on the XRD pattern, most of the nickel oxide in the samples probably exists in such particles. In addition to the nickel oxide particles, relatively large  $\text{LiCrO}_2$  shards were detected (Figs. S4d and S5b). The TEM images did not reveal much new information, as mixed morphologies grown onto impurities dominated the sample (Figs. S6a and S6b). However, a few longer nanotubes or nanofibers were detected (Figs. S6c and S6d). The more defectious material compared to the new nickel samples is supported by the Raman results.

### 3.3.3. Stainless steel

Changing the nickel cathode to a stainless steel cathode had a significant impact on the material produced. Whereas most of the structures in the nickel samples could be categorized as somewhat spherical, the stainless steel sample was strongly dominated by tubular structures, while no nano-onions were found. Fig. 7 shows typical SEM and TEM images from the stainless steel sample.

Figs. 7a and 7b are a good representation of the imaged sample area. Some of the structures were still somewhat spherical, but even those tended to form more chain-like structures and are mixed up with the nanotubes. On the other hand, large areas are found with merely nanotubes, forming a so-called nanotube wool. Further SEM images can

be found in Fig. S7, where higher magnification images of chain-like structures and nanotube wool are presented.

As Fig. 7c shows, a considerable part of the material still consisted of irregularly shaped agglomerates with an impurity seed. However, a significant portion of the material was in nanotube form. The spectrum of different types of nanotubes was reasonably large. Some of them were straight and some very tangled, and the diameters ranged from a few tens of nanometers to a couple hundred nanometers, expressing varying wall thicknesses. Most of the tubes were at least partially filled in the core with material released from the electrodes, with the degree of filling also varying strongly. As a general rule, the straighter tubes seemed to be more filled on average compared to the tangled ones which often contained mostly single particles in their core or at the tip of the tube. Further TEM images of nanotubes and other structures can be found in Fig. S8.

EDS was used with TEM to study the composition of the nanotubes. Fig. 8 shows EDS maps of a few nanotubes for the principal elements.

As the dark-field TEM image clearly indicates, the nanotube in the foreground has a hollow core in the imaged area, whereas the tubes further back contain mostly a solid core consisting of a denser material. As would be expected, the hollow-core nanotube only gave a noticeable

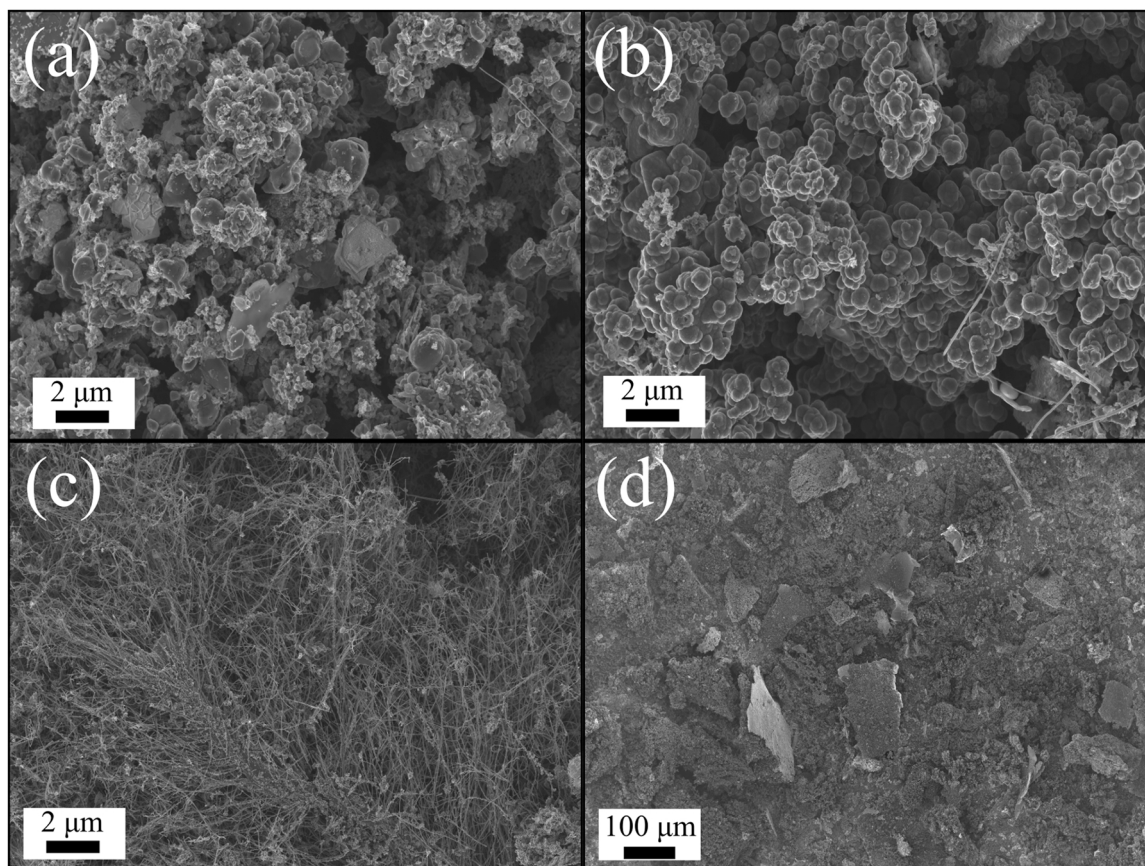


Fig. 9. SEM images of the galvanized steel sample. The sample contained (a) irregular structures, (b) nano-onions, (c) nanotubes and (d) large carbon pieces.

**Table 3**

Product masses from all the experiments. In all the experiments the salt used was  $\text{Li}_2\text{CO}_3$ , temperature was  $750^\circ\text{C}$ , and electrolysis time was 90 min. Cathode material varied. The theoretical maximum amount of carbon produced in one experiment is 1.47 g, as calculated based on Eq. (6). Carbon produced during the  $U/I$  sequence is considered in the theoretical maximum weight.

Experiment	Washed sample mass, (g)
Nickel 1	0.95
Nickel 2	1.33
Used nickel 1	1.22
Used nickel 2	1.70
Stainless steel 1	1.38
Stainless steel 2	1.36
Galvanized steel 1	1.36
Galvanized steel 2	1.45

signal for carbon. Because the structures are quite small, the signals emanating from them are very weak. However, an iron signal could be distinguished coming from the solid core. A very minor nickel signal comes from a part of the vertical nanotube, but based on the results, the core seems to principally consist of iron. This is consistent in light of the emergence of nanotubes, when the nickel cathode was replaced with a stainless steel cathode. Iron seems to be the key factor here in their formation.

### 3.3.4. Galvanized steel

The galvanized steel samples can be best characterized as a combination of the samples produced with other cathodes but dominated by irregularly shaped morphologies. Fig. 9 shows different structures observed in the sample.

Fig. 9a presents the majority of the sample area. There were some distinct morphologies, but they were frequently mixed with other more irregularly shaped structures. Some nano-onions could be found (Fig. 9b), but they were far scarcer and impure compared to the nickel cathode sample. Areas of nanotube wool were also found (Fig. 9c), which strengthens the hypothesis of the role of iron in nanotube formation. Another notable finding was a considerable number of larger carbon pieces, which is an issue already discussed when considering nickel cathodes (Figs. S1c and S1d). The TEM images (Fig. S9) did not provide much significant new information. However, for an unknown reason, high magnification images or EDS measurements could not be performed, as the sample was heavily influenced by the electron beam.

### 3.4. Sample mass

Washed sample masses are shown in Table 3. Previous publications, e.g. [8], have reported high, over 95%, yield for the similar high-temperature molten salt electrolysis discussed here. The product purity has been reported to be 95% and over [8]. Here, the product purity is inferior, as the amounts of impurities are estimated to be higher based on a correlation found between the sample masses and XRD results. The weight fractions of different phases in the sample are somewhat represented by the integrated areas of the XRD peaks. The area of the main graphite peak compared to the combined area of other peaks can be used as an indicator for the carbon fraction. As already discussed along with XRD results, Rietveld analysis for determining absolute fractions is difficult for this type of mixed samples. Thus, the exact amount of the impurities could not be determined, resulting in an inability to determine the exact yield for the process.

For both steel cathodes, the masses of the parallel samples are very close to each other, which correlates well with the similar XRD patterns

observed. Clear differences can be observed between the samples for both nickel cathodes, for both masses and XRD patterns. Thus, it seems that the amount of carbon in parallel samples could be fairly similar whereas the amount of impurities varied more. Based on that, an assumption about the yields being constant between parallel experiments can be made.

#### 4. Conclusions

Molten lithium carbonate electrolysis was used to capture CO<sub>2</sub> and reduce it to solid carbon. An Inconel 625 vessel acted both as a reactor vessel and as an anode. The cathodes used were clean nickel, used nickel, stainless steel, and galvanized steel.

It was observed that different metals dissolved from the electrodes affect the carbon produced and its morphology. Different metals and varying amounts seem to have different types of effects. With little to no dissolved metals mixed with the product, spherical structures were dominant. These spherical, onion-like structures were the main product with unused nickel cathode. With used nickel cathodes product morphology was more various, as more metal was released. With the presence of iron, tubular structures were dominant, as iron acted as a nucleation seed for tube growth. Tubular structures were found when steel-based cathodes, both stainless and galvanized steel, were used. As a general rule it seems that impurities cause inconsistent product containing various carbon morphologies.

As well as the carbon morphology, impurities also affect the size and graphitization degree of the carbonaceous product. Particles with higher amounts of impurities seem to be thinner compared to ones with less impurities. Nanotubes produced with steel cathodes releasing iron seem to have the highest degree of graphitization. In practice, this could indicate that the quality of the product in terms of crystallization can be improved with dissolved iron.

Comparing the sample masses and XRD patterns, it seems that the amount of impurities might vary more than the mass of carbon. This may be an indication that the yields between parallel experiments are fairly similar. To determine yields more accurately, other analysis methods must be utilized.

On the basis of the results of this work, it can be concluded that electrode material selection is crucial for accurate control of the quality and yield of the carbon production by molten salt electrolysis. Metal dissolution to the system does not need to be prevented completely, although it should be carefully controlled, as the dissolved metals clearly have an effect on the product. One possible aspect of the future studies related to these dissolved metals would be to apply specifically selected seed particles to the salt, and by that control the product morphology.

#### CRedit authorship contribution statement

**Emma Laasonen:** Conceptualization, Formal analysis, Investigation, Validation, Writing – original draft, Writing – review & editing. **Miika Sorvali:** Formal analysis, Writing – original draft, Writing – review & editing. **Vesa Ruuskanen:** Conceptualization, Software, Formal analysis, Validation, Writing – original draft, Writing – review & editing. **Markku Niemelä:** Conceptualization, Writing – review & editing. **Tuomas Koironen:** Conceptualization, Writing – review & editing, Supervision, Project administration, Funding acquisition. **Jero Ahola:** Conceptualization, Writing – review & editing, Project administration, Funding acquisition. **Jyrki M. Mäkelä:** Writing – review & editing. **Tero Joronen:** Writing – review & editing, Project administration, Funding acquisition.

#### Declaration of Competing Interest

The authors declare that they have no known competing financial interests or personal relationships that could have appeared to influence the work reported in this paper.

#### Data availability

Data will be made available on request.

#### Acknowledgments

Jane and Aatos Erkko Foundation and the Technology Industries of Finland Centennial Foundation are acknowledged for financial support of the Neo-Carbon Materials project and Business Finland is acknowledged for financial support of the HYGCEL Hydrogen and Carbon Value Chains in Green Electrification project. The authors want to thank Mr. Toni Kangasmäki and Mr. Jose Löyttyinen for their contribution to the reactor design and construction. The authors would also like to thank Mr. Simon Tanter for his contribution to the experimental work during his Erasmus+ internship. The authors also want to thank D.Sc. Mari Honkanen, D.Sc. Turkka Salminen and Mr. Leo Hyvärinen for operating the characterization equipment. This work made use of Tampere Microscopy Center facilities at Tampere University.

#### Appendix A. Supporting information

Supplementary data associated with this article can be found in the online version at doi:10.1016/j.jcou.2023.102390.

#### References

- [1] S. Arcaro, F.A. Berutti, A.K. Alves, C.P. Bergmann, MWCNTs produced by electrolysis of molten carbonate: characteristics of the cathodic products grown on galvanized steel and nickel chrome electrodes, *Appl. Surf. Sci.* 466 (2019) 367–374, <https://doi.org/10.1016/j.apsusc.2018.10.055>.
- [2] J. Ren, S. Licht, Tracking airborne CO<sub>2</sub> mitigation and low cost transformation into valuable carbon nanotubes, *Sci. Rep.* 6 (2016) 1–11, <https://doi.org/10.1038/srep27760>.
- [3] S. Licht, A. Douglas, J. Ren, R. Carter, M. Lefler, C.L. Pint, Carbon nanotubes produced from ambient carbon dioxide for environmentally sustainable lithium-ion and sodium-ion battery anodes, *ACS Cent. Sci.* 2 (3) (2016) 162–168, <https://doi.org/10.1021/acscentsci.5b00400>.
- [4] A. Yu, G. Ma, L. Zhu, Y. Hu, R. Zhang, H.-Y. Hsu, P. Peng, F.-F. Li, Electrochemically controlled in situ conversion of CO<sub>2</sub> to defective carbon nanotubes for enhanced H<sub>2</sub>O<sub>2</sub> production, *Nanoscale* 13 (37) (2021) 15973–15980, <https://doi.org/10.1039/D1NR04176B>.
- [5] P. Wang, M. Wang, J. Lu, Electrochemical conversion of CO<sub>2</sub> into value-added carbon with desirable structures via molten carbonates electrolysis, *RSC Adv.* 11 (46) (2021) 28535–28541, <https://doi.org/10.1039/D1RA03890G>.
- [6] J. Ren, F.-F. Li, J. Lau, L. González-Urbina, S. Licht, One-pot synthesis of carbon nanofibers from CO<sub>2</sub>, *Nano Lett.* 15 (9) (2015) 6142–6148, <https://doi.org/10.1021/acs.nanolett.5b02427>.
- [7] X. Liu, J. Ren, G. Licht, X. Wang, S. Licht, Carbon nano-onions made directly from CO<sub>2</sub> by molten electrolysis for greenhouse gas mitigation, *Adv. Sustain. Syst.* 3 (10) (2019), 1900056, <https://doi.org/10.1002/advs.201900056>.
- [8] X. Liu, X. Wang, G. Licht, S. Licht, Transformation of the greenhouse gas carbon dioxide to graphene, *J. CO<sub>2</sub> Util.* 36 (2020) 288–294, <https://doi.org/10.1016/j.jcou.2019.11.019>.
- [9] L. Hu, Y. Song, S. Jiao, Y. Liu, J. Ge, H. Jiao, J. Zhu, J. Wang, H. Zhu, D.J. Fray, Direct conversion of greenhouse gas CO<sub>2</sub> into graphene via molten salts electrolysis, *ChemSusChem* 9 (6) (2016) 588–594, <https://doi.org/10.1002/cssc.201501591>.
- [10] X. Wang, G. Licht, X. Liu, S. Licht, One pot facile transformation of CO<sub>2</sub> to an unusual 3-D nano-scaffold morphology of carbon, *Sci. Rep.* 10 (1) (2020) 21518, <https://doi.org/10.1038/s41598-020-78258-7>.
- [11] A. Yu, G. Ma, J. Jiang, Y. Hu, M. Su, W. Long, S. Gao, H.-Y. Hsu, P. Peng, F.-F. Li, Bio-inspired and eco-friendly synthesis of 3D spongy meso-microporous carbons from CO<sub>2</sub> for supercapacitors, *Chem. Eur. J.* 27 (40) (2021) 10405–10412, <https://doi.org/10.1002/chem.202100998>.
- [12] A. Yu, G. Ma, L. Zhu, R. Zhang, Y. Li, S. Yang, H.-Y. Hsu, P. Peng, F.-F. Li, Conversion of CO<sub>2</sub> to defective porous carbons in one electro-redox cycle for boosting electrocatalytic H<sub>2</sub>O<sub>2</sub> production, *Appl. Catal. B Environ.* 307 (2022), 121161, <https://doi.org/10.1016/j.apcatb.2022.121161>.
- [13] B. Kaplan, H. Groult, A. Barhoun, F. Lantelme, T. Nakajima, V. Gupta, S. Komaba, N. Kumagai, Synthesis and structural characterization of carbon powder by electrolytic reduction of molten Li<sub>2</sub>CO<sub>3</sub>-Na<sub>2</sub>CO<sub>3</sub>-K<sub>2</sub>CO<sub>3</sub>, *J. Electrochem. Soc.* 149 (2002), <https://doi.org/10.1149/1.1464884>.
- [14] K. Le Van, H. Groult, F. Lantelme, M. Dubois, D. Avignat, A. Tressaud, S. Komaba, N. Kumagai, S. Sigrist, Electrochemical formation of carbon nano-powders with various porosities in molten alkali carbonates, *Electrochim. Acta* 54 (19) (2009) 4566–4573, <https://doi.org/10.1016/j.electacta.2009.03.049>.



- [15] H.V. Ijije, C. Sun, G.Z. Chen, Indirect electrochemical reduction of carbon dioxide to carbon nanopowders in molten alkali carbonates: process variables and product properties, *Carbon* 73 (2014), <https://doi.org/10.1016/j.carbon.2014.02.052>.
- [16] S. Licht, B. Wang, S. Ghosh, H. Ayub, D. Jiang, J. Ganley, A. NewSolar, Carbon capture process: solar thermal electrochemical photo (STEP) carbon capture, *J. Phys. Chem. Lett.* 1 (15) (2010) 2363–2368, <https://doi.org/10.1021/jz100829s>.
- [17] F.-F. Li, J. Lau, S. Licht, Sungas instead of syngas: efficient coproduction of CO and H<sub>2</sub> with a single beam of sunlight, *Adv. Sci.* 2 (11) (2015), 1500260, <https://doi.org/10.1002/advs.201500260>.
- [18] V. Kaplan, E. Wachtel, K. Gartsman, Y. Feldman, I. Lubomirsky, Conversion of CO<sub>2</sub> to CO by electrolysis of molten lithium carbonate, *J. Electrochem. Soc.* 157 (2010) B552–B556, <https://doi.org/10.1149/1.3308596>.
- [19] E. Laasonen, V. Ruuskanen, M. Niemelä, T. Koiranen, J. Ahola, Insights into carbon production by CO<sub>2</sub> reduction in molten salt electrolysis in coaxial-type reactor, *J. Environ. Chem. Eng.* 10 (1) (2022), 106933, <https://doi.org/10.1016/j.jece.2021.106933>.
- [20] A. Yu, G. Ma, J. Ren, P. Peng, F.-F. Li, Sustainable carbons and fuels: recent advances of CO<sub>2</sub> conversion in molten salts, *ChemSusChem* 13 (23) (2020) 6229–6245, <https://doi.org/10.1002/cssc.202002060>.
- [21] J. Ren, A. Yu, P. Peng, M. Lefler, F.-F. Li, S. Licht, Recent advances in solar thermal electrochemical process (STEP) for carbon neutral products and high value nanocarbons, *Acc. Chem. Res.* 52 (2019), <https://doi.org/10.1021/acs.accounts.9b00405>.
- [22] I.A. Novoselova, S.V. Kuleshov, A.A. Omel'chuk, Electrochemical CO<sub>2</sub> conversion, in: R. Inamuddin, M.I. Boddula, A. Khan Ahamed (Eds.), *Carbon Dioxide Utilization to Sustainable Energy and Fuels*, Advances in Science, Technology & Innovation, Springer International Publishing, Cham, 2022, pp. 113–136, [https://doi.org/10.1007/978-3-030-72877-9\\_6](https://doi.org/10.1007/978-3-030-72877-9_6) (pp).
- [23] H. Wu, Z. Li, D. Ji, Y. Liu, L. Li, D. Yuan, Z. Zhang, J. Ren, M. Lefler, B. Wang, S. Licht, One-pot synthesis of nanostructured carbon materials from carbon dioxide via electrolysis in molten carbonate salts, *Carbon* 106 (2016) 208–217, <https://doi.org/10.1016/j.carbon.2016.05.031>.
- [24] D. Tang, H. Yin, X. Mao, W. Xiao, D.H. Wang, Effects of applied voltage and temperature on the electrochemical production of carbon powders from CO<sub>2</sub> in molten salt with an inert anode, *Electrochim. Acta* 114 (2013) 567–573, <https://doi.org/10.1016/j.electacta.2013.10.109>.
- [25] G. Hong, Y. Chen, P. Li, J. Zhang, Controlling the growth of single-walled carbon nanotubes on surfaces using metal and non-metal catalysts, *Carbon* 50 (6) (2012) 2067–2082, <https://doi.org/10.1016/j.carbon.2012.01.035>.
- [26] X. Liu, G. Licht, X. Wang, S. Licht, Controlled transition metal nucleated growth of carbon nanotubes by molten electrolysis of CO<sub>2</sub>, *Catalysts* 12 (2) (2022) 137, <https://doi.org/10.3390/catal12020137>.
- [27] X. Liu, G. Licht, X. Wang, S. Licht, Controlled growth of unusual nanocarbon allotropes by molten electrolysis of CO<sub>2</sub>, *Catalysts* 12 (2) (2022) 125, <https://doi.org/10.3390/catal12020125>.
- [28] H.E. Bartlett, K.E. Johnson, Electrolytic reduction and ellingham diagrams for oxy-anion systems, *Can. J. Chem.* 44 (18) (1966) 2119–2129, <https://doi.org/10.1139/v66-321>.
- [29] J. Lau, G. Dey, S. Licht, Thermodynamic assessment of CO<sub>2</sub> to carbon nanofiber transformation for carbon sequestration in a combined cycle gas or a coal power plant, *Energy Convers. Manag.* 122 (2016) 400–410, <https://doi.org/10.1016/j.enconman.2016.06.007>.
- [30] X. Wang, X. Liu, G. Licht, B. Wang, S. Licht, Exploration of alkali cation variation on the synthesis of carbon nanotubes by electrolysis of CO<sub>2</sub> in molten carbonates, *J. CO<sub>2</sub> Util.* 34 (2019) 303–312, <https://doi.org/10.1016/j.jcou.2019.07.007>.
- [31] L. Malard, M. Pimenta, G. Dresselhaus, M. Dresselhaus, Raman spectroscopy in graphene, *Phys. Rep.* 473 (2009) 51–87, <https://doi.org/10.1016/j.physrep.2009.02.003>.
- [32] A.C. Ferrari, D.M. Basko, Raman spectroscopy as a versatile tool for studying the properties of graphene, *Nat. Nanotechnol.* 8 (2013) 235–246, <https://doi.org/10.1038/NNANO.2013.46>.
- [33] A. Ferrari, J. Meyer, V. Scardaci, C. Casiraghi, M. Lazzeri, F. Mauri, S. Piscanec, D. Jiang, K. Novoselov, S. Roth, A. Geim, Raman spectrum of graphene and graphene layers, *Phys. Rev. Lett.* 97 (2006), 187401, <https://doi.org/10.1103/PhysRevLett.97.187401>.
- [34] W. Weng, L. Tang, W. Xiao, Capture and electro-splitting of CO<sub>2</sub> in molten salts, *J. Energy Chem.* 28 (2019) 128–143, <https://doi.org/10.1016/j.jechem.2018.06.012>.